

• Atomic-scale metastable structure formation in nickel-aluminum alloys synthesized far from equilibrium

Zhehao Chen^{1,*}, Aslak J J Fellman¹, Katarzyna Mulewska², Kenichiro Mizohata¹, Davide Gambino^{1,3}, Yanling Ge⁴, Eryang Lu¹, Flyura Djurabekova¹, Andreas Delimitis⁵, Lukasz Kurpaska², Kostas Sarakinos^{1,6}, and Filip Tuomisto¹

1. Department of Physics, University of Helsinki, Helsinki, Finland
2. NOMATEN Centre of Excellence, National Centre for Nuclear Research, st. A. Soltana 7, 05-400 Otwock, Poland
3. Department of Physics, Chemistry and Biology (IFM), Linköping University, Linköping, Sweden
4. VTT Technical Research Centre of Finland, Finland
5. Department of Mechanical and Structural Engineering and Materials Science, University of Stavanger, N-4036 Stavanger, Norway
6. Department of Physics, KTH Royal Institute of Technology, Sweden

*Corresponding author (e-mail: zhehao.chen@helsinki.fi)

Abstract

This study reports a new meta-stable structure in epitaxial nickel-aluminum (Ni-Al) films (Al content up to 24.4 at.%) grown on MgO(001) substrates by magnetron sputtering. Structure probes by XRD, HRTEM and nano-indentation combined with atomistic simulations consistently demonstrate that in thin film samples with coexisting γ and γ' phases, domains of the two phases are homogeneously intermixed at the atomic-scale, forming a coherent matched lattice with one overall lattice parameter. It expands as aluminum (Al) concentration increases, with γ phase domains being progressively replaced by γ' phase domains. This behavior is similar to a solid solution, where the atomic-scale domain of the γ and γ' phases act as solute and solvent, respectively. Isothermal annealing and nanoindentation reveal that the structure decomposes into distinct γ' and γ phases due to the loss of lattice matching at 400 °C, resulting in an increase in hardness. This is followed by further relaxation and domain growth at higher temperatures (600 °C and 800 °C), accompanied by a decrease in hardness. These observations confirm the metastable nature of the nanoscale γ and γ' phases system, enhance the understanding of the Ni-Al alloy system and providing new insights for meta-stable intermetallic thin film synthesis.

1. Introduction

Nickel-aluminum (Ni-Al) alloys—most notably alloys with Al content from ~10 to ~25 at.%—are renowned for their excellent mechanical properties and high-temperature stability, rendering them important for aerospace, automotive, and electronic applications [1-4]. The equilibrium Ni-Al phase diagram [5] predicts the formation of a random face-centered cubic (FCC) solid solution (denoted as γ phase) for Al contents $\lesssim 10$ at.%, while an ordered phase with the L12 crystal structure corresponding to the Ni_3Al compound (denoted as γ' phase) forms for Al contents ≈ 25 at.%. In the Al content range ~10 to ~25 at.% discrete γ and γ' phase domains coexist, forming coherent interfaces due to their small lattice mismatch ($< 0.5\%$) [6] [7]. This microstructure further contributes to the alloy strength, creep, and corrosion resistance and has been the primary focus of research work [8] [9-11] pertaining to the Ni-Al system.

Alloying—a key route for developing materials with tailor-made properties within physical metallurgy—has been extensively explored through equilibrium synthesis. Concurrently, contemporary materials science and technology has been increasingly relying on non-equilibrium synthesis routes in which quenching [14] large external pressures [15] and atom-by-atom growth of thin films from the vapor phase [16] impose limited atomic-assembly kinetics that enable formation of metastable phases and configurations beyond the predictions of thermodynamics. For the case of Ni-Al alloys, quenching has been a commonly used non-equilibrium synthetic route [17-23] [24, 25]. It has been shown that variation of the solidification rate can significantly affect the microstructure transition and phase development, e.g., by reducing grain

size, increasing dislocation density, and generating fine antiphase domain (APD) structures [17, 20, 22, 26] that enhance ductility [27, 28], the lack of which is one of the main challenges faced by contemporary Ni-Al alloys [ref].

Physical vapor deposition is an effective way to synthesize metastable solid solutions and self-organized nanostructures. Examples include metal nitride, carbide, and boride multinary systems, [2, 29-33] which exhibit (among other features) unique mechanical properties and high-temperature stability behavior [34, 35]. Magnetron sputtering [16, 36, 37], a physical vapor deposition technique that has rapidly developed since the 1980s, is now well-established for industrial production of films and coatings. It is also a very far-from-equilibrium process offering cooling rates of $\approx 10^{14} \text{Ks}^{-1}$ [38] upon vapor condensation, which is several orders of magnitude larger than that achieved by quenching. The effect of such extreme cooling rates on the structure formation of Ni-Al alloy films, its potential for leading to metastable phases and configurations, and its implications for thermal stability and mechanical properties remain largely unexplored.

In the present work, we set out to study structure formation, stability, and mechanical strength of sputtered-deposited thin Ni-Al films. We elect to synthesize epitaxial layers on MgO substrates for Al contents in the range 0 to ~ 25 at. %, such that effects of grain boundaries on phase formation and stability are minimized. Using structure and composition probes, along with theoretical calculations, we show that the films consist of a atomic-scale network of nanometer-size γ and γ' domains. This network exhibits a single and common to both phase domains lattice parameter that progressively

expands with increasing Al content. Furthermore, the γ/γ' domain structure withstand annealing up to a temperature of 873 K at which it decomposes by the formation of distinct γ and γ' domains. Mechanical properties evaluation shows that the film hardness increases from ~ 1.5 GPa to ~ 3.0 GPa with increasing Al content from ~ 7 at. % to ~ 24 at. %. Moreover, annealing initially causes increase in hardness (for a given Al content) followed by softening for annealing temperatures coinciding with the decomposition of the coherent metastable γ/γ' structure. We argue that the initial annealing-induced hardening is caused by lattice matching loss, while the softening is associated with domain coarsening when the structure separates into distinct γ and γ' domains. The overall results of our study are further confirmation that non-equilibrium thin-film synthesis is an effective route for synthesizing metastable materials with structure and properties beyond the predictions of thermodynamics. It also provides new insights into the Ni-Al system and the synthesis of other metastable intermetallic thin films.

2. Research methodology

2.1. Thin-film synthesis and characterization

Ni and Ni-Al layers with various Al contents are deposited epitaxially by magnetron co-sputtering on $10 \times 10 \times 1$ mm³ MgO (001) substrates in an ultrahigh vacuum deposition system (base pressure $\approx 10^{-6}$ Pa), equipped with a load-lock chamber and three magnetron sources. The substrates are cleaned with trichloroethylene, acetone, and ethanol for 10 minutes each and are dried with N₂. Immediately after cleaning, the substrates are mounted on a Mo holder, introduced to the deposition chamber, annealed to 1073K for 60 minutes, and subsequently cooled to the deposition

temperature of 473K. The substrate is heated using radiation from a resistive heater placed less than 5 mm behind the substrate holder. Since the MgO substrate is transparent, a tungsten plate is positioned behind the substrate to absorb the radiation generated by the resistive heater and transfer it via direct contact to the substrate. The substrate temperature is monitored by a thermocouple placed between the substrate and the heater.

Ar (99.99% purity) is used as the sputtering gas, and the discharge pressure is maintained at 0.66 Pa during deposition. Ni and Al targets (purity 99.995%; diameter 50.8 mm) are used for the deposition process. Radio frequency (RF) power (150 W) is applied on the Ni target, while the Al target is operated in direct current (DC) mode with the power ranging from 0 to 51 W is to deposit layers with different Al content. The substrate is rotated at a constant speed of 3 rpm to obtain uniform deposition over the substrate area. Under the synthesis conditions outlined above, and with a target-to-sample distance of 190 mm, the deposition rate is in the range $0.06 - 0.08 \text{ nms}^{-1}$, as measured by a quartz crystal microbalance (QCM) and confirmed by transmission electron microscopy (TEM). The deposition time is 3000 s to achieve a film thickness in the range 180 – 250 nm.

The global elemental composition of the films is determined by time-of-flight elastic recoil detection analysis (ToF-ERDA) in the EGP-10-II 5 MV tandem accelerator of the Helsinki Accelerator Laboratory [39]. Measurements are performed using a 50 MeV ^{127}I ion beam, with the detector positioned at an angle of 40° with respect to the direction of the incident beam, while the beam incident direction forms an angle of 20° with respect to the sample surface. Compositions are calculated using stopping forces

obtained from the SRIM freeware [40], the measurement geometry, and Rutherford elastic recoil cross sections for the detected elements.

High-resolution x-ray diffractometry (XRD) measurements are conducted with a Rigaku SmartLab X-ray diffractometer, employing Cu $K_{\alpha,\beta}$ radiation and a Ge (220) monochromator for studying the film phase composition and crystal structure. Measurements performed in $\theta - 2\theta$ geometry (2θ range 10-90°) show that all layers grow along the $\langle 100 \rangle$ direction exhibiting maxima that correspond to the Ni₃Al (100) and Ni (200) reflections (see Section 3 for details). Based on those reflections, the out-of-plane lattice parameters of the various phases are computed. XRD measurements are also performed in rocking curve ($\omega - \text{scan}$) geometry around the (200) reflection of the layers, while pole figures are also collected with respect to the positions of the (111) and (200) Ni-Al layer reflections.

A JIB-4700F focused ion beam (FIB) system, capable of performing scanning electron microscopy (SEM), energy dispersive x-ray spectroscopy (EDS), and electron backscatter diffraction (EBSD), is utilized to examine the film morphology, determine elemental distribution, and prepare cross-sectional lamellae for transmission electron microscopy (TEM) analyses [41, 42]. The TEM lift-out procedure is performed on the surface region with the area of interest covered by a platinum (Pt) protective layer to prevent further ion damage before lamella lift-out. The lamella is subsequently thinned to approximately 100 nm by ion milling and polishing and is attached to a molybdenum grid for high-temperature annealing preparation. The coarse milling process employs a 30 keV gallium (Ga) ion beam with a current of 500 pA, followed by a fine polishing

stage using a 5 keV Ga ion beam with a current of 30 pA to remove the amorphous layer and additional damage introduced during thinning.

The general microstructure, crystalline structure, and phase composition of the films is investigated using high-resolution TEM (HRTEM), EDS, selected area diffraction (SAD), and dark-field imaging in a JEOL JEM-2800 instrument, equipped with an Energy Dispersive X-ray Spectroscopy (EDS) detector and operated at 200 kV. To facilitate accurate interpretation of HRTEM data with respect to the atomic positions and crystal symmetry, we simulate the images using the AbTEM algorithm [43]. The simulation sample is constructed by creating a two-phase sample comprising both L12 Ni₃Al and fcc Ni structures with dimensions 114×57×890 nm³. The simulation parameters are chosen to reflect the experimental setup and listed in the Supporting Information (Section S1) [ref].

Elastic modulus and hardness of xxxx....

Selected Ni-Al samples are subjected to in-vacuum isothermal annealing (using the deposition chamber) with the purpose of studying the thermal stability of the film structure and crystalline phases. Annealing is performed at temperatures of 673K and 873K for one hour with the base pressure being in the range of 10⁻⁴ to 10⁻⁵ Pa, followed by XRD measurements. The samples also undergo NI analysis to correlate annealing-induced changes in the film microstructure with their mechanical properties.

2.2. Theoretical calculations

To further understand the evolution of the Ni-Al out-of-plane lattice parameters vs. Al content calculated experimentally from XRD, we perform static (i.e., 0K) density functional theory (DFT) and classical molecular dynamics (MD) calculations of random substitutional solid solutions and ordered structures for different Ni-Al alloys in the Al content range 0 to 25 at. %. Random solid solution structures are created by using a pure Ni FCC cell as a starting point and randomly replacing Ni by Al atoms. Ordered systems are created starting from the L12 Ni₃Al structure and replacing Al by Ni atoms. This process depletes the amount of Al in the system while retaining some local ordering. This procedure allows us to control the Al concentration while having some of the atoms in the L12 ordering locally. The lattice parameters are estimated by calculating the energy of the system with different volumes and by solving the equilibrium lattice constant using the Murnaghan equation of state [42].

DFT calculations are performed for cells containing 108 atoms arranged either in fcc random Ni-Al solid-solutions or in the L12 Ni₃Al structure. Due to system size limitations, Al-deficient Ni₃Al-type cells are not considered for DFT calculations. All DFT calculations are performed within the VASP simulation package [45-47] [ref]. We use the PBE GGA exchange-correlation function [48] and projector augmented wave (PAW) pseudopotentials (Al, Ni_pv). The plane-wave expansion energy cutoff is 650 eV for all elements. K-points are defined using Γ -centered Monkhorst–Pack grids with maximum k-spacing of 0.15 \AA^{-1} . Moreover, we apply a first order Methfessel-Paxton smearing of 0.1 eV [49].

MD calculations are performed within the LAMMPS freeware [50] The simulation cells consist of 4000 atoms and interatomic forces are computed using a recently-

developed machine-learned potential for AlCrCuFeNi (publication in preparation). The interatomic potential is based on the Gaussian approximation method [A. P. Bartók, M. C. Payne, R. Kondor, and G. Csányi, *Physical Review Letters* 104, 10.1103/PhysRevLett.104.136403 (2010).] and it is a low dimensional tabulated version (tabGAP) thereof [51, 52] The model uses an external repulsive potential, along with a two-body descriptor, a three-body descriptor, and an EAM-like descriptor. The model has been trained on an extensive database of DFT calculated structures that includes the constituent binary alloys (such as the Ni-Al in the present work). The model is based on the elemental Ni and Al data from recent single element tabGAP potentials [arXiv preprint arXiv:2408.15779]. Initial tests showed that the original formulation of the interatomic potential underestimates the lattice constants of the Ni-Al alloys with reference to DFT calculations. This is to be expected since the model is not explicitly designed for the binary Ni-Al system. Hence, the model has been improved to match DFT lattice constant predictions by modifying its hyperparameters. The list of the hyperparameters of the refitted model are presented in the Supporting Information (Section S2) [ref].

3. Results and discussion.

Figure S1 in Supporting Information [ref] plots the evolution of the Al content (as determined by ToF-ERDA measurements) in the Ni-Al films as a function of the power applied to the Al sputtering cathode. ToF-ERDA analysis also shows that besides Ni and Al, the deposited layers contain minute amounts of impurities (C, O, and H) with a total content less than 1 at. %. In the remainder of the article, we discuss the crystal structure and phase composition of Ni and Ni-Al films, whereby the latter are denoted as Ni_{100-x}Al_x with x being the Al content in at. %.

Figure 1 presents the x-ray $\theta - 2\theta$ diffraction patterns (intensity in logarithmic scale) of Ni and Ni_{1-x}Al_x films. Panel (a) shows patterns in the 2θ range 10 – 90°, along with the angular position of key reflections for the bulk unstrained NaCl-type MgO, fcc Ni, and L12 Ni₃Al [ref] which are marked with vertical dashed lines. The MgO (200) peak emanating from the substrate is observed in all patterns. Moreover, two additional peaks are visible: (i) for all samples a peak at an approximate angular position of 52° in close proximity to the Ni(200) and Ni₃Al(200) reflections; and (ii) for Ni_{1-x}Al_x films with $x \geq 11.4$ at. % a peak at an approximate angular position of 25° closely matching the Ni₃Al(100) reflection region. Since no other peaks are observed in Fig.1 (a), we conclude that our layers exhibit an out-of-plane texture along the $\langle 100 \rangle$ crystallographic orientation. This finding, along with pole figure and rocking curve measurements (representative data for Ni are shown in Fig.S2 in the Supporting Information [ref]) establish that our Ni and Ni_{1-x}Al_x layers grow epitaxially on MgO(100) substrates with orientation relationships $(001)_{\text{Ni}} \parallel (001)_{\text{MgO}}$; $[100]_{\text{Ni}} \parallel [100]_{\text{MgO}}$ and $(001)_{\text{Ni}_{1-x}\text{Al}_x} \parallel (001)_{\text{MgO}}$; $[100]_{\text{Ni}_{1-x}\text{Al}_x} \parallel [100]_{\text{MgO}}$. Epitaxial growth of Ni on MgO(100) has been previously observed by Nakai *et al.* [53] and Milosevic *et al.* [54]. despite the large lattice mismatch (17 %) and has been explained by the formation of a periodic array of misfit dislocations at the film-substrate interface. It is likely that a similar mechanism also facilitates epitaxial growth of Ni_{1-x}Al_x films, however detailed study of the interface structure and its effect on film growth is beyond the scope of the present article.

To further understand the effect of Al content on the film crystal structure and phase composition, magnified areas in the 2θ angular ranges of 23.5° – 26.5° and 49° – 54° are presented in Fig.1 panels (b) and (c), respectively. Figure 1 (b) confirms that the $\text{Ni}_3\text{Al}(100)$ peak only appears for $x \geq 11.4$ at. %. Furthermore, with increasing Al the peak marginally shifts from $2\theta = 25.04^\circ$ at $x = 11.7$ at. % to $2\theta = 25.0^\circ$ at $x = 24.4$ at. %. Concurrently, the Al content increase causes the peak to become sharper, with the full width at half maximum (FWHM) decreasing from 0.62° to 0.27° . Turning to Fig.1 (c), we observe that the peak gradually shifts from the Ni (200) position at $2\theta = 51.91^\circ$ for $x = 0$ to nearly the Ni_3Al (200) position ($2\theta = 51.24^\circ$) for the $\text{Ni}_{75.6}\text{Al}_{24.4}$ sample.

The angular position of the (100) and (200) XRD peaks seen in Fig.1 is used to calculate the out-of-plane lattice parameters of the $\text{Ni}_{1-x}\text{Al}_x$ layers. The results are plotted as function of the Al content in Fig.2, whereby blue filled triangles correspond to data from the (100) XRD reflection and black filled circles correspond to data from the (200) XRD reflection. The lattice parameter increases in a nearly linear fashion up to an Al content of ~ 12 at. % above which the increase becomes seemingly sub-linear. Lattice parameter data—extracted using the machine learned AlCrCuFeNi interatomic potential—of Ni-Al alloys with the γ -NiAl random solid-solution (blue hollow triangles) and the ordered γ' - Ni_3Al (red hollow diamonds) structures are also plotted in Fig.2, along with data from DFT calculations (blue and red hollow stars). The results from the two calculation methods compare favorably, which lends confidence to the accuracy of the semi-empirical force-field model used for capturing the lattice parameter variations as function of Al content. The lattice parameters for the γ -NiAl

and γ' -Ni₃Al ~10 at. %, above which they deviate with the γ -NiAl growing exponentially and its γ' -Ni₃Al counterpart exhibiting a sub-linear evolution. Comparison of experimental and computational data show a consistent evolution as a function of the Al content, whereby ~12 at. % Al the experimental lattice parameter converges towards the computed γ' -Ni₃Al value.

The overall evolution of the XRD diffraction patterns in Fig.1 and the lattice parameters in Fig.2 indicate that for Al contents $x \leq 7.4$ at% the films form a γ – NiAl random solid-solution, while for $x \geq 11.2$ at% γ and the ordered γ' – Ni₃Al phases coexist for with a continuous γ -to- γ' transition upon Al content increase. The fact that the (200) peak between the Ni (200) and Ni₃Al (200) reflections remain symmetric without visible sign of split or deconvolution into multiple peaks implies that the crystal structure is characterized by a single lattice parameter formed by intermixed γ and γ' domains the size of which is sufficiently small to allow for a formation of a coherent structure without the domains relaxing to their equilibrium lattice parameter . Moreover, Fig.1 shows that the (200) peak broadens for intermediate values in the x range 0 to 24.4 at. % relative to the peak shape at the extreme x values, i.e., FWHM is equal to 0.28°, 0.42°, and 0.36° for Al contents of 0, 16.8, and 24.4 at. %, respectively. This is indicative of lattice distortion and strain when both phases coexist and form a coherent network.

TEM analysis is performed to obtain nanoscale information about the crystal structure of the deposited layers and correlate it with the structure and phase formation picture established by the XRD data and the theoretical calculations. Figure 3 shows cross-sectional TEM images and SAD patterns of the Ni_{1-x}Al_x thin films for $x =$

0, 5.3, 14.2, and 24.4 at. %. The bright-field images in Figs.3 (a) through (d) illustrate the overall structure of the films and the MgO substrate (film thicknesses ranging from 100 to 200 nm), from which we establish that the film structure is uniform, and the film/substrate interface is continuous with no signs of extended defected regions. Figures 3 (a1) and (a2) show the SAD patterns of the Ni films and the Ni/MgO interface along the [100] zone axis. The patterns exhibit square symmetry (consistent with the FCC and NaCl-type structure of Ni and MgO). In Fig.3 (a2) the reflection patterns from both Ni and MgO are marked by blue solid and red square, respectively. These two patterns exhibit coherent alignment, indicating high-quality epitaxial growth on the MgO substrate along the [100] direction. Similar features are observed in the SAD patterns for the Ni_{94.7}Al_{5.3} (panels (b1) and (b2)), Ni_{85.8}Al_{14.2} (panels (c2) and (c3)), and Ni_{76.6}Al_{24.4} (panels (d2) and (d3)) samples. Moreover, additional superlattice spots are observed in the SAD patterns corresponding to the Ni_{85.8}Al_{14.2} and Ni_{76.6}Al_{24.4} samples (the (0 – 11) spot is marked with dashed white circles in panels (c2) and (d2)) which indicates formation of the γ' – Ni₃Al structure coexisting with the fcc γ – NiAl solid solution. The marked superlattice reflections are used to perform dark-field (DF) imaging with the objective of identifying areas of segregated Ni₃Al phase, as such segregation is commonly observed in metallurgically synthesized alloys [55]. The DF images are displayed in Figs. 3 (c1) and (d1) showing a uniform structure with no segregation. This finding correlates well with STEM-EDX data that show uniform distribution of Ni and Al in both Ni_{85.8}Al_{14.2} and Ni_{76.6}Al_{24.4} samples (Figs. 3 (c4)-(c6) and (d4-d6)). The overall conclusion of the data presented in Fig.3 is that both γ – NiAl and γ' – Ni₃Al phases are distributed uniformly in the film.

High resolution TEM (HRTEM) is performed with the purpose of understanding the way by which γ – NiAl and γ' – Ni₃Al phases are dispersed in the crystal lattice of the Ni_{1-x}Al_x films. HRTEM images from Ni_{1-x}Al_x samples for x = 0, 5.3, 14.2, and 24.4 at. %, are presented in Figs.4 (a), (b), (c), and (d), respectively, along with the corresponding fast Fourier transform (FFT) as insets. In general, no clear grain boundary observed, and the lattice fringes in all images show high coherency. In the pure Ni and Ni_{94.7}Al_{5.3} samples, the atomic layers are homogeneous, and the difference between [100] and [200] atomic planes is indistinguishable. The FFTs show only the spots corresponding to the fcc structure, indicating that the γ' phase is not significantly present at this low Al content. The images corresponding to the Ni_{85.8}Al_{14.2} and Ni_{75.6}Al_{24.4} films show distinct [100] and [200] atomic planes with weak and bright lattice fringes and superlattice spots of the L12 structure in the FFT, suggesting the formation of γ' phase. For the case of the Ni_{85.8}Al_{14.2} film (Fig.4(c)), the [200] fringes are intermittently visible, suggesting the γ' phase is highly mixed with the γ phase. The domain size of each phase is very small, irregular, and not well defined, indicating a high degree of atomic scale mixing of two phases. In contrast, the image for the Ni_{75.6}Al_{24.4} film (Fig.4(d))—which is close to the stoichiometric Ni₃Al composition—shows a much more distinct and uniform γ' phase. The atomic layers are more ordered, with clear and continuous [100] and [200] fringes, indicating less intermixing with the γ phase compared to the Ni_{85.8}Al_{14.2} sample. This is also supported by the superlattice spots in the FFT pattern, which are brighter and sharper.

In Fig.4 (c), a typical region that contains both γ' and γ phases is marked with a red rectangular and is enlarged in Fig.4 (c3) for further analysis. The image set of Fig.4

(c1) through (c4) shows the supercell model (panel (c1)) used for image simulation (see Section 2 for details), the corresponding simulated HRTEM image (panel (c2)), the experimental HRTEM image (panel (c3)), and the comparison of the experimental and simulated intensity profiles obtained across the γ'/γ interface from experimental and simulated images (panel (c4)). The simulated HRTEM image using mixed γ' and γ supercell model matches well with the experimental HRTEM image (Fig.4 (c1)-(c3)), which provides evidence in favor of the coherent dispersion of the two phases, as marked in orange and red rectangular boxes in Fig.4 (c3).

The intensity profiles in Fig.4 (c4) show that the [100] interplanar spacing is the same for both phases. This provides further support to the notion (according to the XRD data in Fig.1) that the crystal lattice exhibits a single lattice parameter. Moreover, a distinct transition zone from the γ' phase to the γ phase is observed, measuring approximately 1.40 nm, equivalent to about eight atomic [002] planes. This width is in agreement with our image simulations and very close to the thermal equilibrium value of 1.23 ± 0.19 nm reported by Forghani *et al.* [7]. In this transition zone, the lattice is distorted, and coherent structure forms by contraction/expansion of the γ'/γ phase lattice planes. For a unit cell of either phase to relax to its unstrained lattice parameter, the domain radius should be much larger than the transition zone of 1.4 nm. This is not the case as, e.g., seen in Fig. 4(c) where both γ' and γ phase domains are ultra-fine and intermixed at the atomic scale.

Closer inspection of the intensity profile in Fig.4 (c4) shows that the absolute lattice parameter measured by HRTEM (3.51 Å) is 0.04 Å (i.e., 1.1%) smaller than the value determined by XRD measurement (3.55 Å). This difference is slightly larger than the

typical estimated error (0.5%) of HRTEM reported in [56] for the case of a perfect crystal. Since XRD measurements probe a macroscopic area over the entire sample, the observed difference could be explained by local lattice strain, combined with the calibration error in TEM.

The HRTEM image in Fig.4 (c3) exhibits a distinct structural feature marked by the white dashed rectangular box. This feature can be explained as atomic phase misalignment, where part of the γ' phase shifts along $\frac{1}{2} [1\bar{1}0]$ direction, leading to an anti-phase boundary that is perpendicular to the beam direction $[001]$. This is a common type of planar defect in $\gamma' - \text{Ni}_3\text{Al}$ phase [57], whereby the original γ' phase pattern overlaps with the shifted γ' phase pattern.

In summary, the X-ray diffraction (XRD), transmission electron microscopy (TEM), and theoretical energy minimizations consistently indicate that in our thin film samples with Al concentrations within the range in which γ and γ' phases coexist, yield a coherent lattice in which nanometer-size γ and γ' phase domain are homogeneously intermixed at the atomic scale. The lattice parameters from each phase coherently match with each other as an integral lattice structure, resulting in high lattice distortion. The overall lattice parameter gradually expands as the aluminum (Al) concentration increases, with the γ phase being progressively substituted by the γ' phase. This behavior resembles that of a solid solution, wherein the solute units are the unit cells of the γ and γ' phases.

The structure derived from the combined experimental and theoretical analyses is potentially metastable due to the limited diffusion of Ni and Al adatoms caused by the ultrafast cooling rates during vapor condensation in the sputtering process. To validate this hypothesis, the $\text{Ni}_{85.8}\text{Al}_{14.2}$ sample was annealed at 400 °C, 600 °C, and 800 °C. The XRD patterns, reduced modulus and hardness (via nanoindentation), and surface morphology (via SEM) of the annealed samples are presented in Fig. 5.

The XRD patterns (Fig. 5a1–a3) reveal that upon annealing at 400 °C, the (100) peak broadens and shifts slightly to the left at 24.90°, approaching the γ' reference peak position, while the (200) peak remains largely unchanged. Annealing at 600 °C results in a further leftward shift of the (100) peak to 24.87° and a more pronounced sharpening compared to the diffraction pattern at 400 °C, indicating reduced lattice distortion. Simultaneously, the (200) peak becomes asymmetric and can be deconvoluted into two distinct peaks located at 50.97° and 51.57°, respectively. The peak at 50.97° aligns closely with the γ' (200) peak at 51.18°, while the peak at 51.57° corresponds to the as-deposited $\text{Ni}_{85.8}\text{Al}_{14.2}$ sample, indicative of the saturated γ solid solution phase. Annealing at 800 °C causes the (100) peak to broaden further and shift slightly rightward to 24.92°, approaching the bulk Ni_3Al (100) peak at 24.94°. The (200) peak remains asymmetric; however, the γ' (200) peak on the right shoulder becomes too broad to identify accurately, while the γ (200) peak shifts to 51.65°, closer to the original (200) reflection of the as-deposited $\text{Ni}_{92.6}\text{Al}_{7.4}$ sample at 51.70°. This observation suggests a greater formation of the γ' structure. Furthermore, a split peak is observed in the (111) reflection region, indicating a loss of epitaxial growth.

Figure 5b presents the reduced modulus and hardness measurements obtained via nanoindentation at maximum depth of 40 nm. The hardness of the as-deposited Ni_{85.8}Al_{14.2} film is comparable to the near stoichiometric Ni_{24.4}Al_{75.6}. After annealing at 200 °C, the hardness initially increases to 6.03 GPa but gradually decreases to 3.98 GPa as the temperature reaches 800 °C. A similar non-monotonic trend is observed in the reduced modulus. Figure 5c shows the EBSD and EDS data acquired via SEM. The elemental distribution remains homogeneous across all annealing temperatures, while EBSD analysis indicates the formation of large (111) twins grains during annealing at 800 °C. Notably, no elemental separation is observed within the (111) grains.

By comparing the results in Fig. 5, we can observe key changes in the structural and mechanical properties during the annealing process. Since the as-deposited sample exhibits epitaxial growth, grain boundaries are not a concern. Before annealing, the γ' and γ phases shared the same lattice parameter, indicating minimal lattice mismatch at the domain boundary. This contributes to lower hardness. Upon annealing at 400 °C, the lattices of the two phases began to relax, as evidenced in Fig. 5a1 by the shift of the Ni₃Al (100) peak toward the reference peak position. This shift reflects an increasing lattice mismatch between the two phases, which impedes dislocation motion and thereby increases hardness. With further annealing, the (200) peak begins to split into two distinct peaks, representing further lattice relaxation and domain coarsening of the γ' and γ phases. The subsequent decrease in hardness can be attributed to the reduction in domain boundaries as domain size increases. After annealing at 800 °C, the domains of the two phases coarsen further, leading to the loss of epitaxial growth. This is apparent from the appearance of an additional peak in the (111) region (Fig. 5a3) and the observation of large twinned grains in the EBSD

results (Fig. 5c10). Since the grain size exceeds 100 μm , the contribution of grain boundaries to the hardness remains negligible.

4. Summary and conclusions

This study reports a new metastable structure in the Ni-Al system, synthesized via magnetron sputtering. X-ray diffraction, transmission electron microscopy, and theoretical calculations demonstrate that the γ' and γ phases are intermixed at the atomic level, forming a coherent lattice with a single parameter. As the aluminum content increases, γ phase domains are progressively replaced by γ' phase domains. This behavior resembles a solid solution, where the atomic-scale domains of γ and γ' act as solute and solvent, respectively.

Isothermal annealing combined with nanoindentation measurements reveals that the coherent structure decomposes into distinct γ' and γ phases at 400 °C due to the loss of lattice matching—resulting in increased hardness. Further relaxation and domain growth occur at 600 °C and 800 °C, causing the hardness to decrease. Overall, these findings deepen our understanding of the Ni-Al alloy system and provide new insights for synthesizing metastable intermetallic thin films.

Figures and figure captions

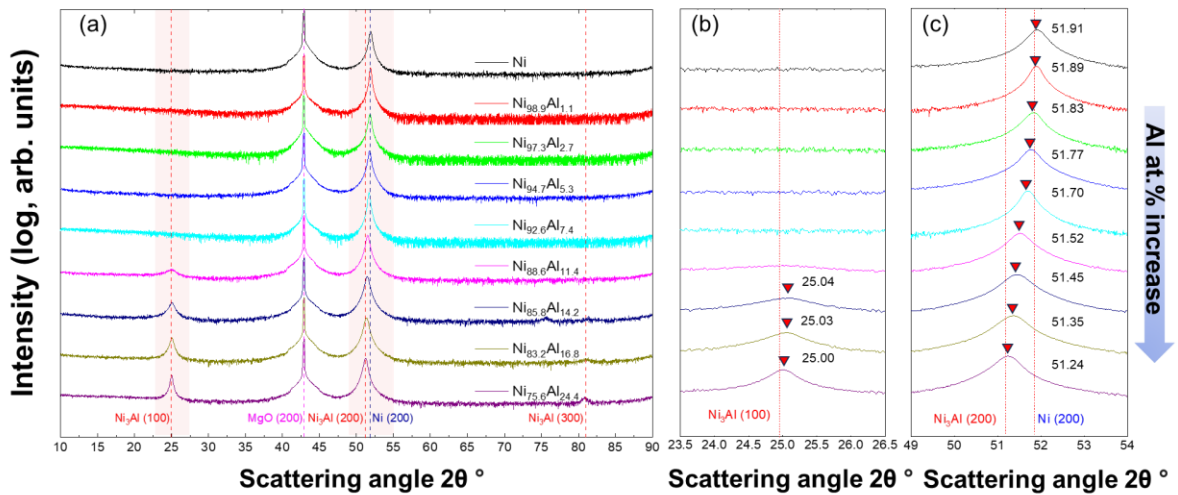


Fig.1. XRD patterns of Ni and Ni_{1-x}Al_x films. Panel (a) shows patterns in the 2θ angle range 10 – 90°, while panels (b) and (c) present magnified regions in the 23.5 – 26.5° and 49 – 54° ranges, respectively. The vertical dashed lines in all panels indicate the angular position of reflections for the bulk unstrained MgO, Ni, and Ni₃Al. In (b) and (c) red arrows mark the peaks in the respective diffraction patterns, with the angular position provided next to each pattern.

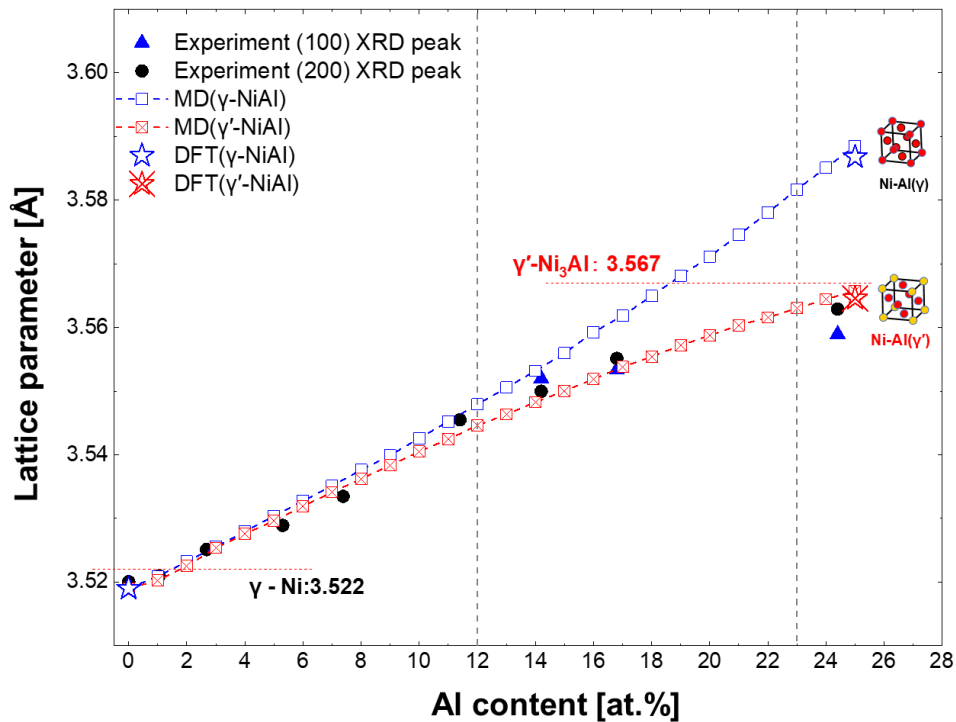


Fig.2 Lattice parameter of the Ni_{1-x}Al_x films vs. Al content x, as measured experimentally (filled symbols) and determined from DFT calculations and MD simulations. The blue filled triangles and back circles correspond to lattice parameter values determined from the angular position of (100) and (200) XRD peaks, as presented in Fig.1. The blue hollow triangles and the red diamonds show the lattice parameters calculated from MD simulations for Ni-Al alloys with the γ -NiAl random solid-solution and the ordered γ' -Ni₃Al structures, respectively. The blue and red hollow stars correspond to lattice parameter values calculated by DFT for Ni-Al alloys with the γ -NiAl and γ' -Ni₃Al structure, respectively. The dashed lines connecting the data points from MD simulations are guides to the eye only.

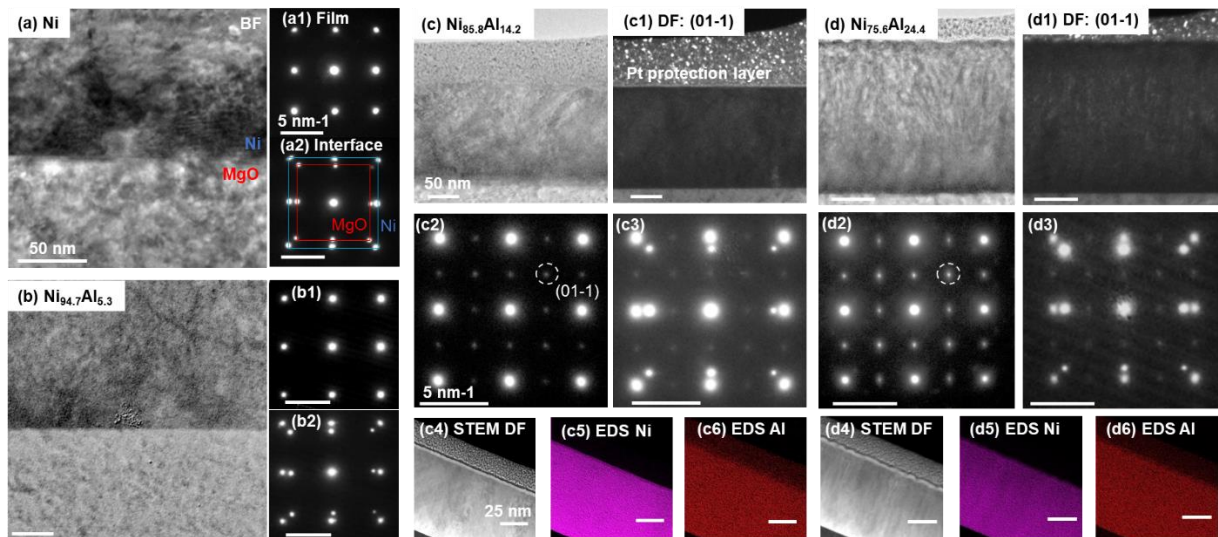


Fig.3. Transmission electron microscopy (TEM) images, selected area diffraction (SAD) patterns, and element distribution of $\text{Ni}_{1-x}\text{Al}_x$ thin films for $x = 0, 5.3, 14.2,$ and 24.4 at. %. Panels (a-d) show bright-field (BF) TEM images of the films and interfaces, with a scale bar of 50 nm. Panels (a1 and a2), (b1 and b2), (c2 and c3), and (d2 and d3) display SAD patterns of the film and interface regions along the $[100]$ zone axis, with a scale bar of 5 nm^{-1} . The SAD patterns from the film (Ni) and the substrate (MgO) are marked by blue and yellow squares in (a2). Panels (c1) and (d1) present dark-field (DF) micrographs from $\text{Ni}_{85.8}\text{Al}_{14.2}$ and $\text{Ni}_{75.6}\text{Al}_{24.4}$ films, respectively. The DF micrographs are recorded using the (011) superlattice reflection of the Ni_3Al structure (marked with a dashed circle in panel (c1) and (d1) with a scale bar of 50 nm). Panels (c4-c6) and (d4-d6) show dark-field scanning TEM (STEM) images and Energy Dispersive X-ray Spectroscopy (EDS) elemental mapping of Ni and Al, with a scale bar of 25 nm.

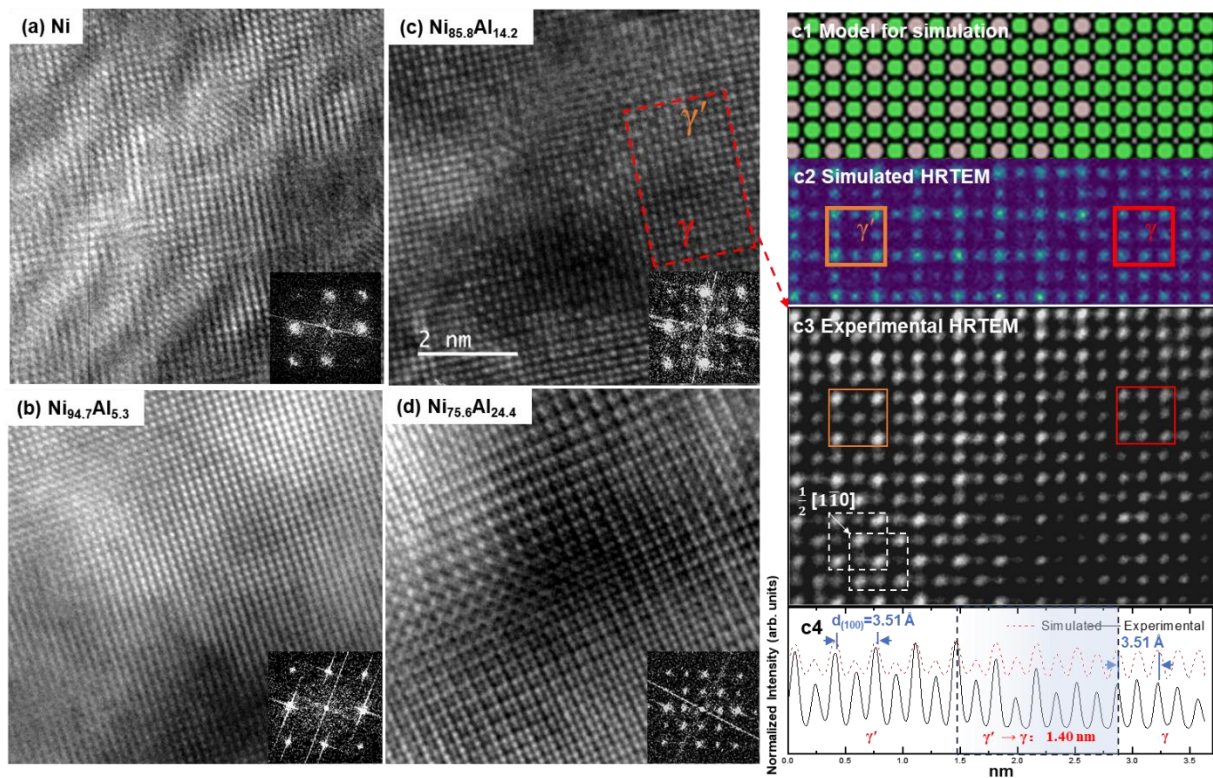


Fig.4. High-resolution TEM (HRTEM) images with FFT analysis of Ni_{1-x}Al_x films compared to simulated images along the (100) zone axis. Panels (a-d) display HRTEM images of Ni_{1-x}Al_x thin films for x = 0, 5.3, 14.2, and 24.4 at. %, respectively, along with corresponding FFT insets. The scale bar for all images is 2 nm. Panel (c3) shows an enlarged HRTEM image from panel (c), compared with a simulated HRTEM image (c2) and the corresponding model of a Ni₃Al and Ni mixed super-cell (c1). The orange, red, and white dashed boxes indicate the γ' , γ , and γ' phases shifted along the $\frac{1}{2}$ $[1\bar{1}0]$ direction, respectively. Panel (c4) compares the integrated bright intensity profiles along the γ' to γ phase from the experimental (c1) and simulated (c2) images. The scale of panels (c1-c4) is indicated on the horizontal axis in panel (c4).

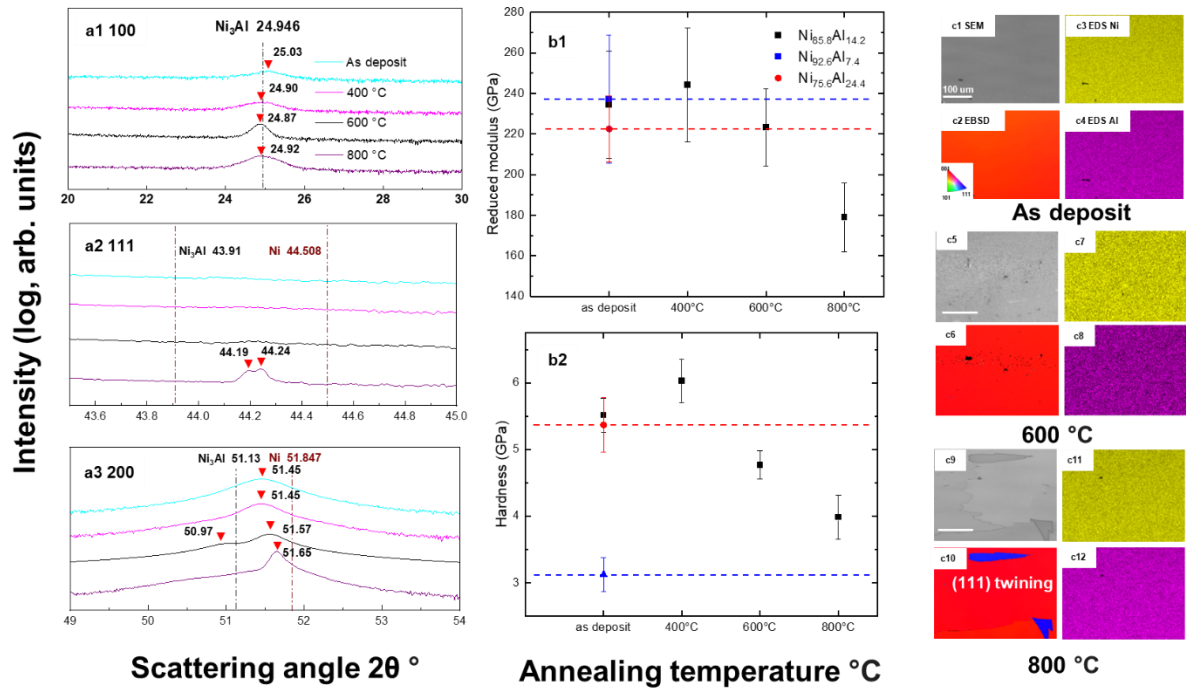


Fig.5. (a1-a3) XRD patterns of as-deposited and annealed at 400, 600 °C and 800 °C $\text{Ni}_{85.8}\text{Al}_{14.2}$ films. Panels (a1), (a2) and (a3) present magnified regions from 100, 111 and 200 diffraction ranges for Ni_3Al and Ni, respectively. The vertical dashed lines in all panels indicate the angular position of reflections for the Ni and Ni_3Al . In (a1), (a2) and (a3) red arrows mark the peaks in the respective diffraction patterns, with the angular position provided next to each pattern. Panel sections b1 and b2 shows the reduced modulus and hardness measured by nanoindentation (up to 40 nm depth) of annealed $\text{Ni}_{85.8}\text{Al}_{14.2}$. The as-deposited $\text{Ni}_{92.6}\text{Al}_{7.4}$ and $\text{Ni}_{75.6}\text{Al}_{24.4}$ are used as reference for solid solution and stoichiometric Ni_3Al , as marked by blue and dash line. Panel sections (c1), (c2) and (c3) present results from surface and microstructure characterization before and after annealing of the $\text{Ni}_{85.8}\text{Al}_{14.2}$ films. (c1, c5 and c9) Top-view scanning electron microscopy (SEM) images. (c2, c6 and c10) Electron backscatter diffraction (EBSD) inverse pole figure map. (c3, c7 and

c11) and (c4, c8 and c12) Energy-dispersive X-ray spectroscopy (EDS) maps showing elemental distribution of Nickel (Ni) and Aluminum (Al), respectively.

References

- [1] A.R. Paul, M. Mukherjee, D. Singh, A Critical Review on the Properties of Intermetallic Compounds and Their Application in the Modern Manufacturing, *Crystal Research and Technology* 57(3) (2021).
- [2] S.K. Tiwari, A.U. Rao, A.S. Kharb, A.K. Chawla, D.K. Avasthi, A review of mechanical and tribological properties of Ni₃Al-based coatings-synthesis and high-temperature behavior, *Physica Scripta* 98(7) (2023).
- [3] P. Jozwik, W. Polkowski, Z. Bojar, Applications of Ni₃Al Based Intermetallic Alloys—Current Stage and Potential Perceptivities, *Materials* 8(5) (2015) 2537-2568.
- [4] T.M. Pollock, S. Tin, Nickel-Based Superalloys for Advanced Turbine Engines: Chemistry, Microstructure and Properties, *Journal of Propulsion and Power* 22(2) (2006) 361-374.
- [5] <ASM Handbook Vol 3.pdf>.
- [6] X.L. Liu, S.-L. Shang, Y.-J. Hu, Y. Wang, Y. Du, Z.-K. Liu, Insight into γ -Ni/ γ' -Ni₃Al interfacial energy affected by alloying elements, *Materials & Design* 133 (2017) 39-46.
- [7] F. Forghani, J.C. Han, J. Moon, R. Abbaschian, C.G. Park, H.S. Kim, M. Nili-Ahmadabadi, On the control of structural/compositional ratio of coherent order-disorder interfaces, *Journal of Alloys and Compounds* 777 (2019) 1222-1233.
- [8] THE ORDER-DISORDER TRANSFORMATION IN Ni₃Al AND Ni₃Al-Fe ALLOYS-I. DETERMINATION OF THE TRANSITION TEMPERATURES AND THEIR RELATION TO DUCTILITY.
- [9] R.R. Unocic, N. Zhou, L. Kovarik, C. Shen, Y. Wang, M.J. Mills, Dislocation decorrelation and relationship to deformation microtwins during creep of a γ' precipitate strengthened Ni-based superalloy, *Acta Materialia* 59(19) (2011) 7325-7339.
- [10] Ductilization of Ni₃Al by alloying with elements boron and substitutional.
- [11] On the Ductility of the Intermetallic Compound Ni₃Al*.
- [12] Physical and mechanical metallurgy of Ni₃Al and its alloys.
- [13] DUCTILITY AND FRACTURE BEHAVIOR OF POLYCRYSTALLINE Ni₃Al ALLOYS*.
- [14] Y.Q. Cheng, E. Ma, Atomic-level structure and structure–property relationship in metallic glasses, *Progress in Materials Science* 56(4) (2011) 379-473.
- [15] High-Pressure Crystallography: from fundamental phenomena to technological applications[M]. Springer, 2010.
- [16] Martin P M. Handbook of deposition technologies for films and coatings: science, applications and technology[M]. William Andrew, 2009.
- [17] Rapidly Solidified and Annealed Powders of Ni₃Al.
- [18] Chemically disordered Ni₃Al synthesized by rapid solidification: an experimental investigation of the quenching parameters.
- [19] Effects of solidification kinetics on phase selection of Ni–Al alloys.
- [20] Rapid solidification of intermetallic compounds.
- [21] Y.-F. Li, C. Li, J. Wu, H.-J. Li, Y.-C. Liu, H.-P. Wang, Microstructural Feature and Evolution of Rapidly Solidified Ni₃Al-Based Superalloys, *Acta Metallurgica Sinica (English Letters)* 32(6) (2018) 764-770.

- [22] H. Li, L. Zheng, H. Zhang, S. Li, H. Zhang, S. Gong, Effects of solidification parameters on microstructures of Ni3Al based single crystal, *Procedia Engineering* 27 (2012) 1187-1192.
- [23] Y. Li, C. Li, L. Yu, Z. Ma, H. Li, Y. Liu, Characterization of γ' precipitate and γ/γ' interface in polycrystalline Ni3Al-based superalloys, *Vacuum* 176 (2020).
- [24] Processing and operating experience of Ni3Al-based intermetallic.
- [25] PROCESSING, PROPERTIES, AND APPLICATIONS OF NICKEL AND IRON ALUMINIDES.
- [26] Relationship between the APD structure and ductility of rapidly solidified Ni3Al alloys.
- [27] Microstructural changes observed in a rapidly solidified Ni3Al alloy during isothermal treatments.
- [28] Rapidly Solidified and Annealed Powders of Ni3Al.
- [29] METASTABLE COATINGS - PREDICTION OF COMPOSITION AND STRUCTURE.
- [30] F. Rovere, D. Music, S. Ershov, M.t. Baben, H.-G. Fuss, P.H. Mayrhofer, J.M. Schneider, Experimental and computational study on the phase stability of Al-containing cubic transition metal nitrides, *Journal of Physics D: Applied Physics* 43(3) (2010).
- [31] P.H. Mayrhofer, A. Hörling, L. Karlsson, J. Sjöln, T. Larsson, C. Mitterer, L. Hultman, Self-organized nanostructures in the Ti-Al-N system, *Applied Physics Letters* 83(10) (2003) 2049-2051.
- [32] Deposition of epitaxial ternary transition metal carbide films.
- [33] H. Euchner, P.H. Mayrhofer, Designing thin film materials - Ternary borides from first principles, *Thin Solid Films* 583 (2015) 46-49.
- [34] B. Alling, A. Karimi, I.A. Abrikosov, Electronic origin of the isostructural decomposition in cubic $M_{1-x}Al_xN$ ($M=Ti, Cr, Sc, Hf$): A first-principles study, *Surface and Coatings Technology* 203(5-7) (2008) 883-886.
- [35] A. Hörling, L. Hultman, M. Odén, J. Sjöln, L. Karlsson, Mechanical properties and machining performance of $Ti_{1-x}Al_xN$ -coated cutting tools, *Surface and Coatings Technology* 191(2-3) (2005) 384-392.
- [36] S.M. Rosnagel, Magnetron sputtering, *Journal of Vacuum Science & Technology A: Vacuum, Surfaces, and Films* 38(6) (2020).
- [37] G. Bräuer, B. Szyszka, M. Vergöhl, R. Bandorf, Magnetron sputtering – Milestones of 30 years, *Vacuum* 84(12) (2010) 1354-1359.
- [38] MAGNETRON SPUTTERING OF ALLOY-BASED FILMS.
- [39] Comparison of TOF-ERDA and nuclear resonance reaction techniques for range profile measurements of keV energy implants
- [40] J.F. Ziegler, *Srim-2003, Nuclear Instruments and Methods in Physics Research Section B: Beam Interactions with Materials and Atoms* 219-220 (2004) 1027-1036.
- [41] S. Shen, L. Hao, X. Liu, Y. Wang, Y. Li, J. Zhang, E. Fu, The design of Pd-containing high-entropy alloys and their hardening behavior under He ion irradiation, *Acta Materialia* 261 (2023).
- [42] Z. Chen, E. Lu, K. Mizohata, L. Anna, X. An, T. Suhonen, A. Laukkanen, J. Lagerbom, A. Pasanen, A. Vaajoki, F. Tuomisto, Suppression of helium migration in arc-melted and 3D-printed CoCrFeMnNi high entropy alloy, *Journal of Nuclear Materials* 599 (2024).
- [43] Madsen, Jacob, and Toma Susi. "The abTEM code: transmission electron microscopy from first principles." *Open Research Europe* 1 (2021).
- [44] C.L. Fu, K.M. Ho, First-principles calculation of the equilibrium ground-state properties of transition metals: Applications to Nb and Mo, *Physical Review B* 28(10) (1983) 5480-5486.
- [45] G. Kresse, J. Hafner, Ab initio molecular dynamics for liquid metals, *Phys Rev B Condens Matter* 47(1) (1993) 558-561.
- [46] Efficiency of ab-initio total energy calculations for metals and semiconductors using a plane-wave basis set.
- [47] Efficient iterative schemes for ab initio total-energy calculations using a plane-wave basis set.
- [48] Generalized Gradient Approximation Made Simple.
- [49] M. Methfessel, A.T. Paxton, High-precision sampling for Brillouin-zone integration in metals, *Phys Rev B Condens Matter* 40(6) (1989) 3616-3621.

- [50] A.P. Thompson, H.M. Aktulga, R. Berger, D.S. Bolintineanu, W.M. Brown, P.S. Crozier, P.J. in 't Veld, A. Kohlmeyer, S.G. Moore, T.D. Nguyen, R. Shan, M.J. Stevens, J. Tranchida, C. Trott, S.J. Plimpton, LAMMPS - a flexible simulation tool for particle-based materials modeling at the atomic, meso, and continuum scales, *Computer Physics Communications* 271 (2022).
- [51] Byggmästar, Jesper, Kai Nordlund, and Flyura Djurabekova. "Simple machine-learned interatomic potentials for complex alloys." *Physical Review Materials* 6.8 (2022): 083801.
- [52] Byggmästar, Jesper, et al. "Multiscale machine-learning interatomic potentials for ferromagnetic and liquid iron." *Journal of Physics: Condensed Matter* 34.30 (2022): 305402.
- [53] RBS and XHRTEM characterization of epitaxial Ni films prepared by biased d.c. sputter deposition on MgO(001)
- Hisashi.
- [54] E. Milosevic, P. Zheng, D. Gall, Electron Scattering at Epitaxial Ni(001) Surfaces, *IEEE Transactions on Electron Devices* 66(10) (2019) 4326-4330.
- [55] Microstructure and growth modes of stoichiometric NiAl and Ni₃Al thin films deposited by r.f.-magnetron sputtering.
- [56] J. Biskupek, U. Kaiser, Practical considerations on the determination of the accuracy of the lattice parameters measurements from digital recorded diffractograms, *J Electron Microsc (Tokyo)* 53(6) (2004) 601-10.
- [57] A. Lasalmonie, B. Chenal, G. Hug, P. Beauchamp, Structure and anisotropy of antiphase boundaries in rapidly solidified Ni₃Al, *Philosophical Magazine A* 58(3) (1988) 543-554.